



Residual Stress Measurement of Suspension HVOF-Sprayed Alumina Coating via a Hole-Drilling Method

T. A. Owoseni¹ · M. Bai² · N. Curry³ · E. H. Lester¹ · D. M. Grant¹ · T. Hussain¹

Submitted: 2 October 2019 / in revised form: 1 June 2020
© The Author(s) 2020

Abstract The nature and magnitude of residual stresses in thermal-sprayed coatings determine their lifetime and failure mechanisms. The residual stresses of suspension high-velocity oxy-fuel (SHVOF) thermal sprayed alumina (Al_2O_3) coating were measured with hole-drilling and x-ray diffraction. The coating is dense and consists of amorphous and two crystalline phases: alpha and gamma. The residual stresses measured by hole-drilling in the Al_2O_3 coating was -162 MPa (compression) in the longitudinal direction and -104 MPa (compression) in the transverse direction. This is due to the peening stress and the high substrate–coating CTE ratio of ~ 2.1 . The nature of the residual stress through the coating is related to the microstructure build-up shown from the cross section and the fracture surfaces of the coating.

Keywords alumina · hole-drilling · residual stress · SHVOF · thermal-spray coating

Residual Stresses Credit Line: This article is part of a special topical focus in the *Journal of Thermal Spray Technology* on Advanced Residual Stress Analysis in Thermal Spray and Cold Spray Processes. This issue was organized by Dr. Vladimir Luzin, Australian Centre for Neutron Scattering; Dr. Seiji Kuroda, National Institute of Materials Science; Dr. Shuo Yin, Trinity College Dublin; and Dr. Andrew Ang, Swinburne University of Technology.

✉ T. Hussain
tanvir.hussain@nottingham.ac.uk

¹ Faculty of Engineering, University of Nottingham, Nottingham NG7 2RD, UK

² Department of Materials Science and Engineering, University of Sheffield, Sheffield, South Yorkshire, UK

³ Treibacher Industrie AG, Auer-von-Welsbach-Straße 1, 9330 Althofen, Austria

Introduction

Thermal spray is a widely used surface engineering process for coating deposition, which involves propelling melted or partially melted particles onto the surface. Thermal spray coatings can be deposited from most materials: primarily from rod, wire or powder fed into a plasma or a combustion gas as in a flame spray of a high-velocity oxy-fuel (HVOF) thermal spray (Ref 1). Thermal spray is used in depositing ceramic materials for high value engineering applications, for example, Al_2O_3 coatings in electrical insulation, corrosion, and wear applications (Ref 2–4). Suspension spray is a relatively new branch of thermal spray where instead of a dry powder feedstock, suspensions are used. Suspensions are fed into plasma as in suspension plasma spray (SPS) (Ref 5) or into combustion gas in the case of suspension high-velocity oxy-fuel (SHVOF) spray (Ref 6)—both SPS and SHVOF can deposit coatings from sub-micron- to nanometric-size feedstock carried in liquid media.

The overall performance and lifetime of coatings are subject to the magnitude and nature of their residual stresses (Ref 7). The nature of the residual stresses found in thermally sprayed coatings is primarily due to either the deposition process or property mismatch between the coating and the substrate. The deposition process builds the quenching and the peening stress in case of HVOF thermal spray; the property mismatch yields the thermal stresses. The peening stress develops due to the impact velocity of unmolten or partially molten particles impinging overlaid splats. The quenching stress develops as splats reach thermal equilibrium with underlying splats or substrate while the thermal stress forms from the cooling of the coating and the substrate—this may preclude thermal gradients (Ref 8). The quenching stress is tensile and process specific—its magnitude increases with inter-pass coating

thickness and inter-lamellae bond strength (Ref 9). The magnitude of quenching stress reduces by through-thickness yielding as splats spread, intra- and inter-splat micro-cracking and interfacial sliding (Ref 8). The peening stress is compressive given its mode of development—its magnitude can also be reduced by the formation of micro-cracks (Ref 10). The thermal stress, however, can be tensile or compressive depending on the thermal expansion coefficients (CTEs) of the coating and the substrate. The contribution of the thermal stress can be minimized if the substrate/coating CTE ratio is approximately unity—this will reduce the mismatch strain (see Eq 1).

$$\varepsilon = \left(\frac{\alpha_s}{\alpha_c} - 1 \right) \alpha_c \Delta T \quad (\text{Eq 1})$$

where ε is the mismatch strain; ΔT (K) is the temperature change across the coating thickness; and α_c and α_s are the thermal expansion coefficient of the coating and the substrate, respectively.

Stresses, however, are generated in coatings due to the processing technique. Residual stress is the inherent stress in a material keeping it at equilibrium when unloaded (Ref 11). Sintered or hot-isostatic-pressed ceramic composites made from fine particles possess high residual stress. The increased stress originated from reduced inter-particle spacing among the composite components (Ref 12). HVOF-thermal-sprayed Al_2O_3 coating from micron-size powder and spray-dried nanopowder was reported by Bolelli et al. (Ref 13). The magnitude of the x-ray diffraction residual stress in the coating from the nanostructured powder was higher (136 MPa) than 116.5 MPa from the micron-size powder—although in both coatings they remained tensile. In a different work, Bolelli et al. (Ref 14, 15) measured the residual stress of HVOF-sprayed Al_2O_3 coatings deposited from alcohol-based suspension using incremental hole-drilling technique—the coatings showed tensile and compressive stresses. In the first work (Ref 14), the author linked the nature of the stress in the Al_2O_3 coating to deposition efficiency. Coating deposited from suspension with large agglomerates ($D_{50} = 18.3 \mu\text{m}$) has the least deposition efficiency with compressive stress profile averaging (-184 MPa). Two other coatings from suspension of smaller agglomerates ($D_{50} = 1.52 \mu\text{m}$ and $2.89 \mu\text{m}$) are thicker due to increased deposition efficiency; their residual stress profile was tensile with average of 18 and 60 MPa, respectively. In the second work (Ref 15), the residual stress profile of Al_2O_3 coatings deposited from an Al_2O_3 suspensions of micron-size particles ($D_{50} = 1.26 \mu\text{m}$) and another of sub-micron-size particles ($D_{50} = 0.55 \mu\text{m}$) using different spray conditions specified by combustion chamber length and suspension injection mode (gas atomized and mechanical injection) were compressive. Even so, with the same combustion chamber

length (22 mm) and the same suspension, a change in suspension injection mode changed the coating microstructure with accompanied increase in the compressive stress in the coating—the coating made with mechanical injection has -132 MPa , while the other made with gas atomized injections has -238 MPa .

Residual stress measurement techniques vary in their accessibility and precision; they include diffraction techniques (neutron and x-ray), curvature method, focus ion beam milling, hole-drilling and digital image correlation—neutron diffraction technique offered the deepest nondestructive penetration measurement. These techniques measure residual stress in bulk materials and coatings (Ref 16). Thermal spray coatings consist of splats and defects of different types and can have different degree of crystallinity and amorphous contents. None of the residual stress measuring techniques provides enough information on the contribution of each of the thermal spray coating constituents. The x-ray-based nondestructive diffraction technique relies on the dominant crystalline phase in a coating, to calculate its residual strain or stress (Ref 13, 17). This can be improved upon to ensure that we are able to estimate the contribution of each phase in a coating although there has not been any diffraction technique to estimate the contribution of the amorphous phase in thermal-sprayed coatings. Other non-diffraction-based residual stress measuring techniques rather provide the stress in the coatings as a bulk contribution of its constituents (Ref 18, 19). Incremental hole-drilling—a quasi-nondestructive technique—can profile the residual stress of a coating. A major advantage of this technique is its commercial availability, and it has been used by industry practitioners for quality assurance.

Despite Al_2O_3 being widely used and studied engineering ceramics, limited work has been reported on the through-thickness residual stress behavior of SHVOF-thermal-sprayed Al_2O_3 . In our previous work (Ref 20), we have shown the implications of deposition parameters on the wear performance of Al_2O_3 coatings deposited by SHVOF thermal spray process. A detailed understanding of residual stress of the coating will provide further insight into the performance evaluation of the coatings vis-à-vis the role of residual stress. The aim of this paper is to use hole-drilling technique and x-ray diffraction to investigate the residual stresses in SHVOF-thermal-sprayed Al_2O_3 coating deposited with spray parameters optimized for wear applications. The microstructure of the coatings was studied in detail in SEM and XRD to rationalize the residual stress behavior in terms of microstructure.

Experimental

Materials and Coating Deposition

Alumina (Al_2O_3) coating deposited onto AISI 304 stainless steel substrate has been used in this study. The Al_2O_3 coating was sprayed from bespoke aqueous suspension containing ~ 21 wt.% of pure alpha Al_2O_3 powder (CR1 grade, $D_{50} = 1 \mu\text{m}$) sourced from Baikowski (Poisy, France). The AISI 304 cold-rolled stainless steel used as the substrate ($60 \times 25 \times 2$ mm) had a nominal composition of 19.0 Cr-9.3 Ni-0.05 C and Fe (in wt.%).

The coating was sprayed using a modified UTP TopGun SHVOF thermal spray unit from Miller Thermal Inc. (Wisconsin, USA) with axial injection of suspension directly into the combustion chamber with a 0.3-mm nozzle diameter. Table 1 shows the spray parameters for both coatings. The substrates were continuously cooled by compressed air during the deposition of the two coatings using the same cooling protocol to avoid any variation in sample cooling. The cooling protocol ensures the substrate temperature gave a value not more than 200°C , and the substrates get cooled to room temperature in less than a minute after deposition by the compressed air reaching the substrates. The suspension was delivered from a pressurized vessel maintained at 3 bar which resulted in a feed rate of 90 ml/min. The complete setup was further described elsewhere (Ref 21). The suspension was stirred for ~ 6 h at 700 rpm using overhead stirrer-IKA RW20 digital (Wilmington, USA) to homogenize the suspension before spraying. The substrates were grit-blasted at 3 bar with fine alumina particles (0.125–0.149 mm) using a grit blaster from Guyson (Dudley, England). Following grit blasting, the substrates were cleaned in industrial methylated spirit (IMS) in an ultrasonic bath for 10 min and blown dry with compressed air. The substrates were then mounted onto a rotating carousel with a vertical axis of rotation operating at 73 rpm, while the spray gun traversed

along the vertical axis at a speed of 5 mm/s. This resulted in a relative velocity of 1 mm/s on the substrate (Ref 20).

Feedstock and Coatings Characterization

A fractional part of the Al_2O_3 suspension was heated separately in a box furnace at 100°C for 8 h to obtain dried powder for secondary electron (SE) images on the scanning electron microscope (SEM). Cross sections of the coating were prepared by standard metallographic procedures for back-scattered electron (BSE) images on the SEM. Fractured surface of the coating was prepared from notched samples ($5 \times 25 \times 2$ mm) of coated substrates cooled in liquid nitrogen for 5–10 min before being bent in a vice to fracture at the notch. The secondary electron images of the powder, the fractured surfaces and the back-scattered electron images of the coatings cross section were obtained using JEOL 6490 SEM from JEOL Ltd. (Tokyo, Japan).

The powder dried from the suspension and the as-sprayed coating were scanned on a Bruker D500 diffractometer (Siemens, AB, Germany) with a $\text{Cu K}\alpha$ radiation source (1.54 \AA) and a point detector for phase identification. Powders were scanned within 10° – $120^\circ 2\theta$, step of 0.05° and dwell of 4 s for phase analysis. The as-sprayed coating was scanned for phase analysis with 10° – $140^\circ 2\theta$, step of 0.04° and dwell of 16 s. A more detailed scan was executed for the as-sprayed coating to reduce noise in the acquired signals. Quantitative Rietveld refinement of the XRD data was performed with TOPAS (Coelho Software, Australia) to quantify the phases with the crystallite size calculated using fundamental parameters approach and whole powder pattern modeling (WPPM) (Ref 22).

Micro-hardness and Nanohardness Measurement

Micro- and nanoindentations were carried out on the polished cross section of the as-sprayed coating. The micro-hardness was measured in three rows—five on each—at a load of 10 gf on Vickers micro-hardness tester (Buehler, USA). The nanohardness and the reduced elastic modulus of the coating were obtained from the nanoindentation performed on the polished cross section of the coating. The average microhardness and nanohardness of each row were presented with associated standard error in mean. The nanoindentation was carried out at room temperature on the Platform 3 rig produced by Micro Materials Ltd (Wrexham, UK) using a Berkovich indenter tip. The loading–dwell–unloading scheme was used maintaining a peak load of 20 mN for 2 s and a rate of 4 mN/s during loading and unloading stages for a total of 30 indentations per sample in six rows (five in each row) adequately spaced from coating surface and coating–substrate interface. The elastic modulus was then estimated by Oliver and Pharr method (Ref

Table 1 Spray parameters for SHVOF-thermal-sprayed Al_2O_3 coating deposited onto stainless steel substrate

Parameters	Values
Fuel (hydrogen) flow rate, l/min	612
Oxygen flow rate, l/min	306
Flame power, kW	101
Suspension flow rate, ml/min	90
Spray distance, mm	85
Number of passes	41
Spray gun traverse speed, mm/s	5

23) where the reduced elastic modulus of the indenter system E_r , the elastic modulus of the indenter material E_i and the coating elastic modulus E_c are related as in Eq 2.

$$\frac{1}{E_r} = \frac{1 - \nu_c^2}{E_c} + \frac{1 - \nu_i^2}{E_i} \quad (\text{Eq 2})$$

In Eq 1, ν is Poisson's ratio with c and i representing coating and indenter, respectively. The E_i and ν_i are taken as 1140 GPa and 0.07, respectively (Ref 24).

Residual Stress Measurements: Hole-Drilling and X-Ray Diffraction

Through-thickness residual stress profile of the as-sprayed coating was calculated from relaxed strain measured by incremental hole-drilling completed with the Stresscraft Ltd (Loughborough, UK) hole-driller using a diamond-impregnated inverted cone cutter. The measurement setup is shown in Fig. 1. The hole-drilling was completed using the orbital milling method to forestall damage around the drilled hole, yet the microstructure of a thin layer around the hole could change. Also ceramic coatings are susceptible to micro-cracks—this influences residual stress measurement by the hole-drilling method (Ref 17). The relaxed strain was measured by an EA-06-062RE target three-gauge rosette (Vishay Precision Group, Malvern, Pennsylvania, USA). The gauges are radially oriented to be 45° to one another (Ref 25) to ease the mathematical representation of the relationship between the calibration constants, the relaxed strains, and the required stresses (Ref 26). The two perpendicular gauges were oriented: one to record the longitudinal strain (ϵ_1) and another one to record the transverse strain (ϵ_3). Each gauge recorded relaxed strain data at each depth of a 1-mm-diameter hole drilled to 16 incremental depths: of four 32 μm , four 64 μm and eight 128 μm to reach a final hole depth of 1408 μm . The

collected data were analyzed based on the UK National Physical Laboratory (NPL) Measurement Good Practice Guide 53 (Ref 25). The results were interpreted with the Stresscraft RS INT software (v5.1.3) using the integral method described by Schajer (Ref 26). The integral method is the most reliable analytical procedure for the relaxed strain data obtained from incremental drilled hole (Ref 26). The through-thickness residual stresses were evaluated based on the elastic modulus obtained from the nanoindentation tests. The evaluation yielded longitudinal, transverse and shear stresses converted to the maximum and minimum principal stresses using Eq 3a and 3b, respectively.

$$\sigma_{\max} = \frac{\sigma_x + \sigma_y}{2} + \left[\left(\frac{\sigma_x - \sigma_y}{2} \right)^2 + \tau_{xy}^2 \right]^{1/2} \quad (\text{Eq 3a})$$

$$\sigma_{\min} = \frac{\sigma_x + \sigma_y}{2} - \left[\left(\frac{\sigma_x - \sigma_y}{2} \right)^2 + \tau_{xy}^2 \right]^{1/2} \quad (\text{Eq 3b})$$

where σ and τ represent the normal and shear stresses and x and y indicate the longitudinal and the transverse directions, respectively. The average of each of the stresses in the longitudinal and transverse directions was also calculated. All tensile stresses were recorded as positive and the compressive stresses with a negative sign.

The x-ray diffraction residual stress scan of the coating surface was conducted on the D8-Discover (Bruker AXS Inc., Madison, WI, USA) with Cu K α radiation source (1.54 Å); the parameters are stated in Table 2. The defocusing of the diffractometer at tilt angles above zero ($\Psi \neq 0^\circ$) was minimized with the usage of high-diffraction-angle planar reflections (hkl) (Ref 27). The scanned data were then analyzed using Stress 2.0 software (PANalytical, Almelo, The Netherlands). The average XRD residual stress of the two coatings was calculated based on the differential technique that eliminates the need for a reference strain/stress free sample. A linear relationship is evoked between the surface stress in any direction and the

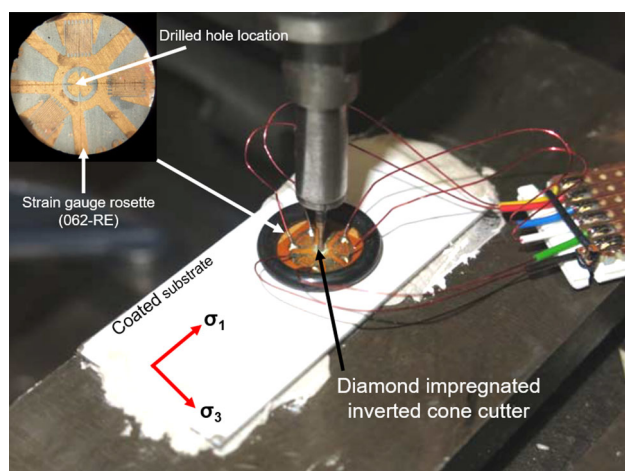


Fig. 1 Incremental hole-drilling residual stress measurement setup

Table 2 XRD residual stress scan parameters

Parameters	Values
2θ , °	139–152
Step size, °	0.1
Dwell time, s/step	8
orientation angle, φ °	0, 45, 90
Tilt angle, ψ °	0–60
PDF card	γ -Al ₂ O ₃ , 00-10-0425
Peak	145.3°

measured interplanar lattice spacing according to Eq 4—the $\sin^2\Psi$ technique (Ref 28).

$$\sigma_\phi = \left(\frac{E}{1+\nu} \right) \frac{1}{d_{(\phi\psi)_0}} \left(\frac{\Delta d_{\phi\psi}}{\Delta \sin^2 \psi} \right) \quad (\text{Eq 4})$$

where $d_{(\phi\psi)_0}$ and $\left(\frac{\Delta d_{\phi\psi}}{\Delta \sin^2 \psi} \right)$ are the intercept and slope of a plot of $d_{\phi\psi}$ against $\sin^2 \psi$ and ν is the Poisson's ratio. E has been used as macroscopic elastic modulus obtained from nanoindentation measurements. The value of E used thus represents an average value over all possible directions in the crystal lattice; this may vary significantly from the diffraction elastic constant due to anisotropy (Ref 29).

Results

Coating Microstructure

Figure 2 and 3 presents the scanning electron micrographs and the phase quantifications of the as-received Al_2O_3

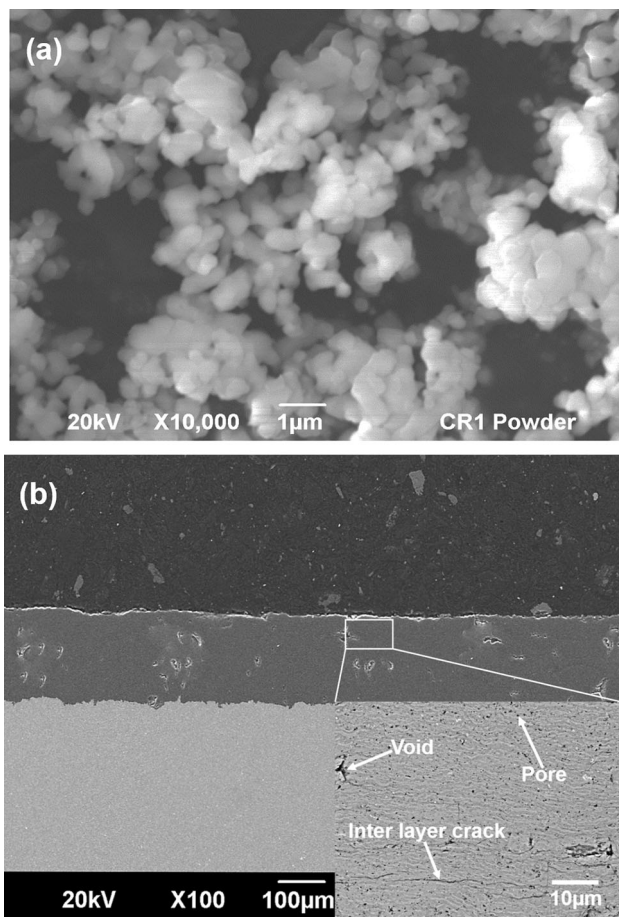


Fig. 2 Al_2O_3 (a) secondary electron high-magnification SEM micrograph of the as-received powder $D_{50} = 1 \mu\text{m}$. (b) Back-scattered electron low-magnification SEM micrograph of the as-sprayed coating with inset showing pores, voids, and inter-layer crack

feedstock and the as-sprayed Al_2O_3 coating. The Al_2O_3 feedstock shown in Fig. 2(a) presents particles of angular morphology with a size range of ~ 100 – 200 nm —the particle size of $1 \mu\text{m}$ provided by the supplier represents the size for agglomerates. The BSE cross-sectional view of the as-sprayed Al_2O_3 coating presented in Fig. 2(b) shows the coating thickness is $\sim 200 \pm 2 \mu\text{m}$ with horizontal cracks and voids at the inter-spray layers. The measured porosity of the Al_2O_3 coating was $5.6 \pm 1.0\%$. The coating–substrate interface shows good bonding without any defect or delamination. The surface roughness of the substrate from the grit blasting offers interlocking sites for the impinging splats. The phase analysis of the powder shown in Fig. 3(a) confirms the as-received powder is entirely corundum (alpha Al_2O_3). The corundum crystallites in the analyzed powder are coarse with calculated size being $141 \pm 4 \text{ nm}$. The signal of aluminum in the phase quantification is from the sample holder used during the powder scan. The phase analysis of the as-sprayed Al_2O_3 coating shown in Fig. 3(b) presents two amorphous humps at the $\sim 40^\circ$ and $60^\circ 2\theta$ positions and two crystalline phases of gamma- Al_2O_3 and corundum. The crystalline contents of the coating have $\sim 19.94\%$ corundum with the balance being gamma- Al_2O_3 which has a crystallite size of $48 \pm 2 \text{ nm}$.

The surface morphology and the fractured surface of the Al_2O_3 coating present different architectures as shown in Fig. 4 and 5. The surface of the coating shown in Fig. 4 is flat, covered by splats of varying geometry and size. Individual splat here is larger than the size of the individual particle in the feedstock; the splats are made up of one or more particle agglomerates. The fractured surface of the coating shown in Fig. 5 revealed different features of the coating lamellae. The morphologies of the lamellae are different than what has been described of SHVOF-thermal-sprayed Al_2O_3 coatings—the lamellae are larger and thicker (Ref 30).

Nanohardness, Indentation Elastic Modulus and Micro-hardness

Figure 6 shows the results of the nanoindentation on the cross section of the as-sprayed Al_2O_3 coating. Figure 6a shows the nanohardness of the Al_2O_3 coating. The nanohardness results on each row show consistent nanohardness except for the third row at a depth of $90 \mu\text{m}$ from the coating top surface—this row has the lowest nanohardness of $9 \pm 1 \text{ GPa}$. The elastic modulus of the Al_2O_3 coating is shown in Fig. 6b. The values plotted in the figure are obtained from Eq 2. The lowest stiffness of the coating is shown at the depth of $90 \mu\text{m}$; the average value at this depth is $171 \pm 15 \text{ GPa}$. The average elastic modulus from the thirty indentations is $200 \pm 7 \text{ GPa}$ —this

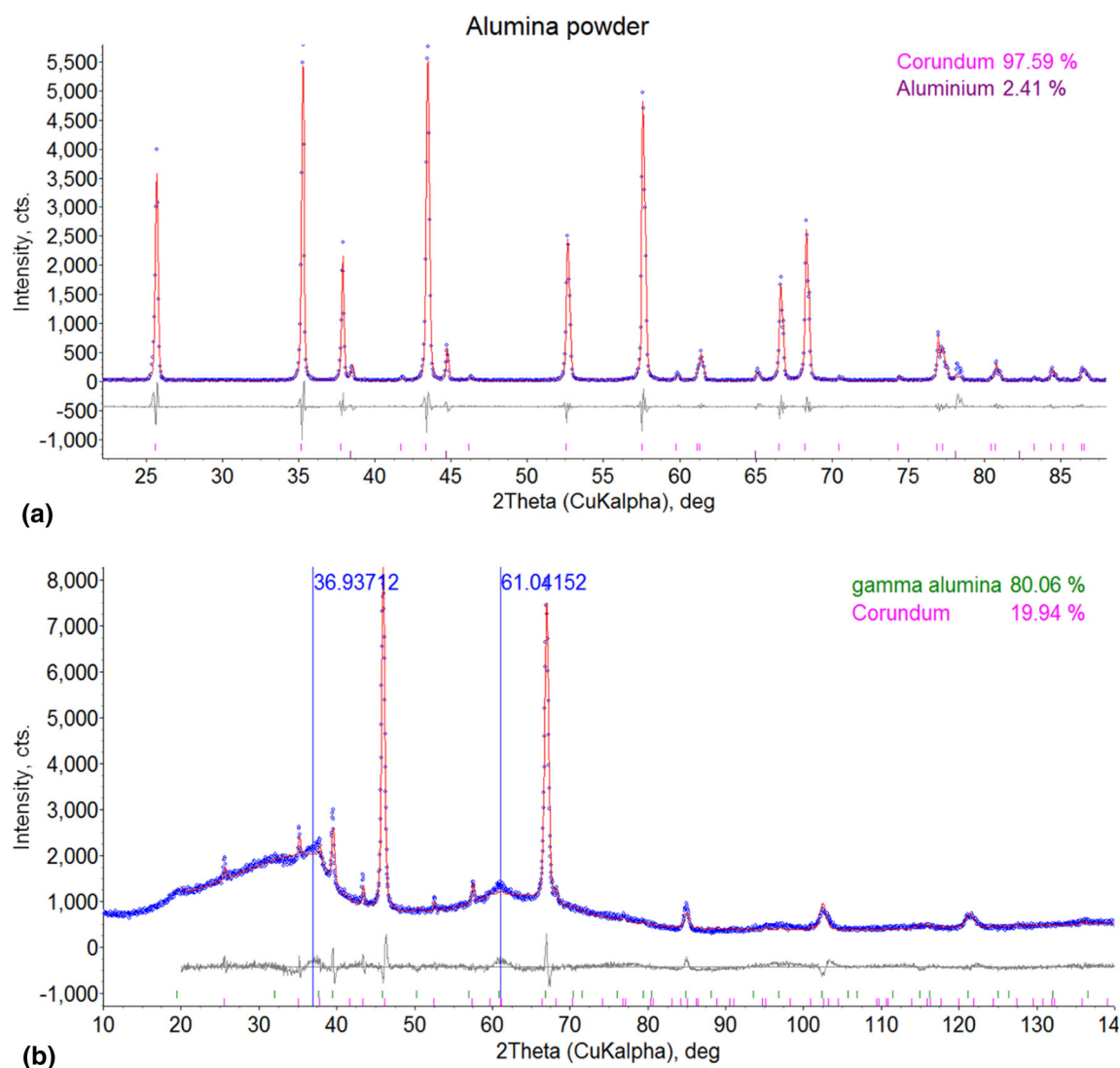


Fig. 3 (a) Rietveld refinement of the as-received powder showing whole α - Al_2O_3 . (b) Rietveld refinement of the as-sprayed coating showing gamma- Al_2O_3 and corundum quantification

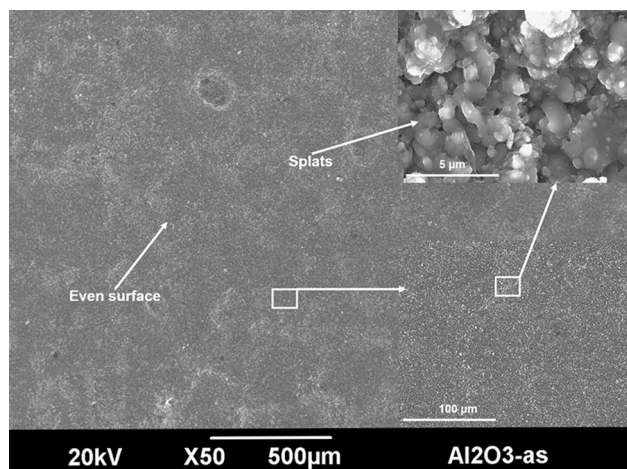


Fig. 4 Surface morphology showing as-sprayed Al_2O_3 coating with even surface covered by splats of varying sizes and geometry

value agrees with the reports of other researchers (Ref 15). The micro-hardness of the as-sprayed Al_2O_3 coating measured on three rows is presented in Fig. 7. Each of the bars represents average of five indentations in a row with the associated standard error in mean. The lowest micro-hardness of the coating (7.4 ± 0.3 GPa) is measured at the depth of 15 μm from its top surface. The effective micro-hardness of the Al_2O_3 coating from fifteen micro-indent comes to 8 ± 0.3 GPa.

Residual Stress Distribution: Hole-Drilling and X-ray Diffraction

The residual stress profile of the Al_2O_3 sample from the hole-drilling is shown in Fig. 8. Figure 8a shows the longitudinal and transverse stresses were compressive near the

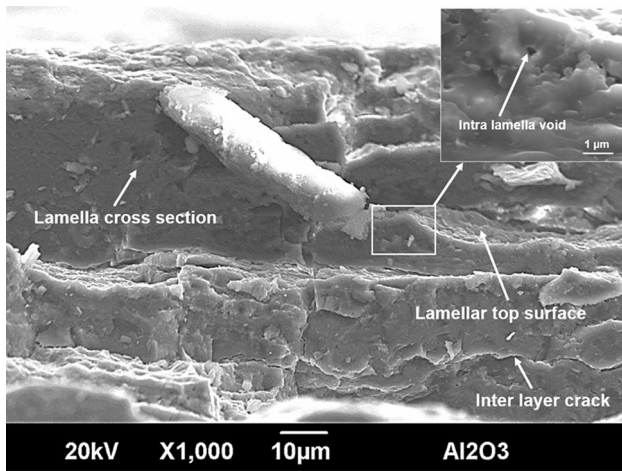


Fig. 5 Fractograph showing lamella cross section, lamella top surface, intra-lamella void, and inter-layer crack in the as-sprayed Al₂O₃ coating

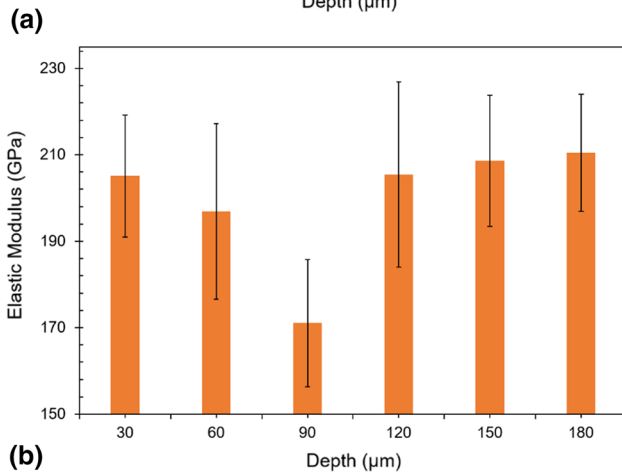
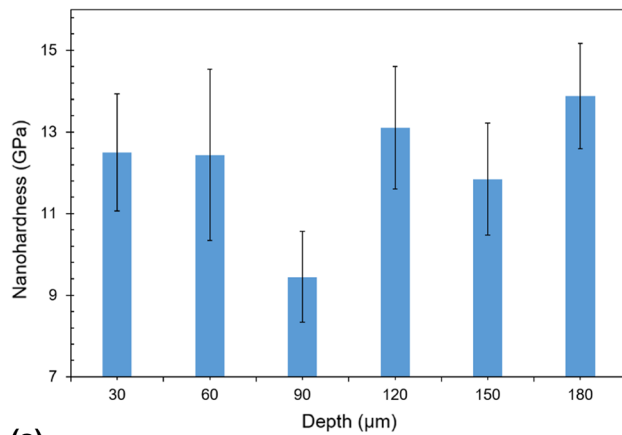


Fig. 6 Depth profile of the (a) nanohardness of the as-sprayed Al₂O₃ coating, (b) Elastic modulus of the as-sprayed Al₂O₃ coating

coating surface. The stresses changed to tensile with increasing depth; the longitudinal stress reached 12 and 219 MPa, while the transverse stress reached 81 and 321 MPa at the 112 and 160 μm depths, respectively. The

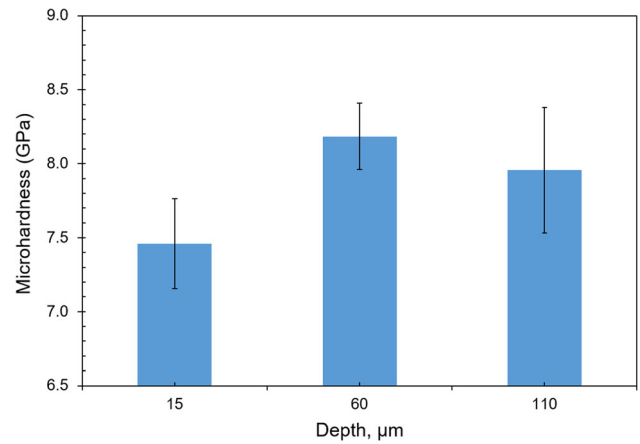
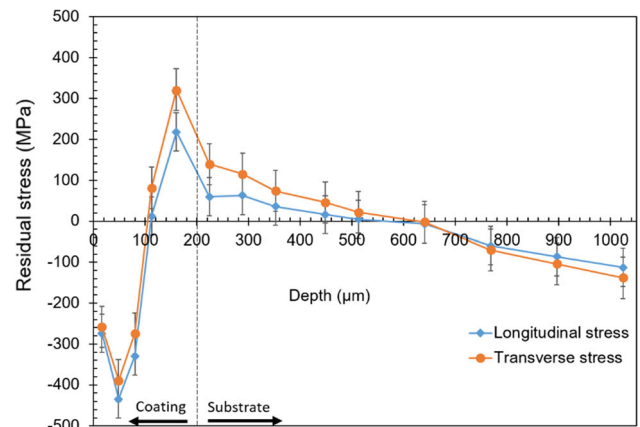
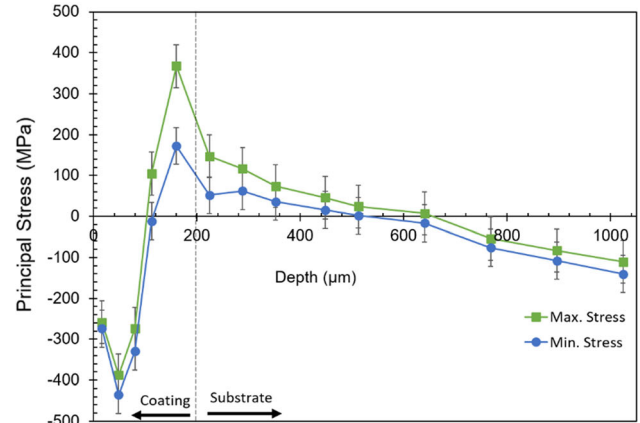


Fig. 7 Depth profile of the micro-hardness of the as-sprayed Al₂O₃ coating



(a)



(b)

Fig. 8 Incremental hole-drilling, (a) longitudinal and transverse residual stresses in the as-sprayed Al₂O₃ coating, (b) principal residual stresses in the as-sprayed Al₂O₃ coating

stress value at the 112 μm depth represents the coating stress state half-way its depth from the top, while the stress value at the 160 μm depth gives the coating stress state near the coating-substrate interface. The stresses in the

substrate changed from tensile to compressive as depth increased. At the depth of 224 μm , the longitudinal stress was 60 MPa; it reached -113 MPa at the 1.02 mm depth. Similarly, the transverse stress was 139 MPa at the depth of 224 μm and has reached -138 MPa at the 1.02 mm depth.

The principal stresses for the Al_2O_3 sample obtained from Eq 3a and 3b show the same trend as the longitudinal and the transverse stresses (Fig. 8b). The maximum and minimum stresses at the 112 μm depth are 105 and -11 MPa, respectively. At the 160 μm depth, the maximum and minimum stresses are both tensile with the values of 367 and 172 MPa, respectively. The maximum and minimum stresses at the midpoint of the substrate (1.02 mm) seem equal to the longitudinal and the transverse stress indicating the shear stress contribution at this depth is negligible.

Figure 9 shows the plot of $d_{\phi\psi}$ against $\sin^2\phi\psi$ for the as-sprayed Al_2O_3 coating measured by x-ray diffraction. The near surface of the Al_2O_3 coating is in a compressive stress state with a magnitude of -8.3 ± 0.2 MPa in the longitudinal direction (σ_{0°) and tensile with a magnitude of 25.3 ± 0.8 MPa in the transverse direction (σ_{90°).

Discussion

Coating Microstructure

The microstructure of the coating reflects the thermal properties of the feedstock from which it was sprayed. The processing parameters used to deposit the coating caused the Al_2O_3 particles to melt, producing coatings with lamellae. The thermal properties of the material, e.g., enthalpy of fusion, are also significant to the microstructure obtained in the coating (Ref 31). The enthalpy of fusion

represents the thermal energy needed to liquefy a solid mass—its magnitude depends on the mass of the substance. The instantaneous thermal energy of the flame varies from the combustion chamber downstream up to the substrate given the temperature gradient established for SHVOF thermal spray process (Ref 32). The hypersonic speed of the combusted gases carrying the particles and the short spray distance (85 mm) suggest the particles have short in-flight time. Therefore, the mass/size of the particles plays a significant role in the resulting microstructure of the coating; small size particles would attain sufficient heating because they will have low enthalpy of fusion. So, in this case, the Al_2O_3 particles are micrometric ($D_{50} = 1 \mu\text{m}$); they would have low enthalpy of fusion. Even though the in-flight time is small, the particles melt to produce dense individual lamella. This is supported by the absence of intra-lamella cracking as shown through the fractograph of the coating. The suspension medium besides processing parameters and material properties determines the physical interaction between the flame and the particles (and molten droplets) in a SHVOF thermal spray process. Aqueous carrier cools the flame as it consumes the thermal energy of the flame due to its high specific enthalpy of vaporization (2.26 MJ/kg), while organic solvents (like ethanol) enhance the energy of the flame with its heat of combustion (Ref 33). Where the evaporation of water or the burning of the ethanol occurs in the combustion chamber, it creates higher chamber pressure that increases combustion gas velocity—this often translates to high particle velocity that yields dense coatings (Ref 33, 34). The spray condition used for the Al_2O_3 coating has been shown by Chadha et al. (Ref 34) to establish this phenomenon. In spite of the cooling of the combusted gas by the aqueous carrier of the Al_2O_3 particles, most of the particles melt to form droplets due to the size of the individual particles in the agglomerates (Ref 35) and the flame temperature being higher than 2100 $^\circ\text{C}$ (Ref 36). The droplets were propelled by the high-velocity combustion gas onto the substrates to form well-adhered splats that built into densely packed lamellae shown on the fractograph of the Al_2O_3 coating. The thickness of the lamellae varies up to 10 μm —the lamellae size range shows these are created from molten agglomerates of the Al_2O_3 particles. The cross section of the lamellae shows non-uniform fine intra-lamella voids. The top surface of the lamella appears smooth. The large size of the lamellae is possibly due to coalescence of droplets. The initial droplets adhere to the substrate due to the improved surface roughness of the substrate achieved from the grit blasting process. Lack of similar level of surface roughness between successive lamellae layers of the coating creates weak bonding between those, resulting in inter-layer cracks in the coating.

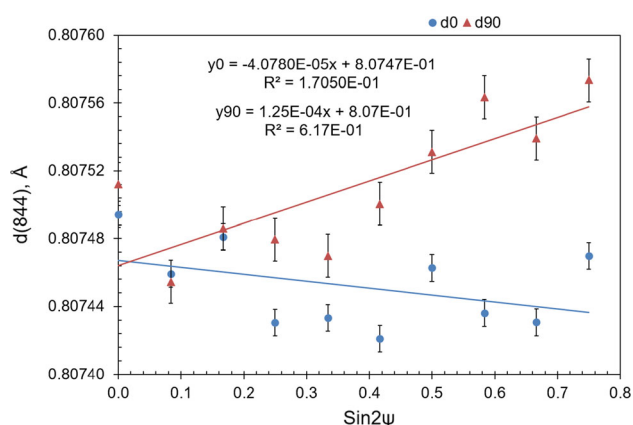


Fig. 9 Plot of d -spacing against $\sin^2\psi$ for the near surface XRD residual stress in the as-sprayed Al_2O_3 coating

The fluid dynamic properties of the suspension medium and its surrounding combustion gas also affect the coating formation from an atomization point of view (Ref 33). This dynamic properties are combined in dimensionless numbers—Weber number (We) and the Reynolds number (Re) (Ref 37). The suspension injection process can be classified as a dense spray process—it has large number of droplets accompanied by disintegration and droplets interactions (Ref 38). While atomization has the primary and secondary regimes, the secondary atomization is the rate-controlling process in a dense spray process because the primary breakup is unstable (Ref 39). We number is mostly considered for the secondary atomization study; its increase changes the breakup regime in succession from bag to catastrophic break up (Ref 40). More so, it can be inferred from the work of Dai and Faeth (Ref 41) that the Re number in the combustion chamber of SHVOF thermal spray gun offers a flow regime where the drag properties of the suspension droplets are unaffected by the viscosity of the combustion gas. The size of the lamellae in the fractograph and the size of the splats from the surface morphology images of the Al_2O_3 coating suggest they were formed from bigger suspension droplets obtainable at the bag breakup level of the secondary atomization—this suggests the We number of the suspension droplets is in the range of 12–50 (Ref 40).

The impact of the thermal treatment on the Al_2O_3 particles caused most of the Al_2O_3 particles to melt to form amorphous Al_2O_3 and gamma- Al_2O_3 although some α - Al_2O_3 was detected in the as-sprayed coating as shown by the XRD results—these are from the unmolten feedstock. The retention of the α - Al_2O_3 could have been due to entrapment during molten droplet formation in-flight or the α - Al_2O_3 particles arrived at the substrate surface and get buried in the large lamellae that form the coating. The particles were, however, undetected in the fractograph due to their sub-micron sizes. In another vein, peak broadening in x-ray diffraction profile reflects crystal imperfections; it occurs due to any or combination of reduced crystallite size, increased dislocation density, stacking faults, twinning, micro-stress, grain boundaries, and chemical heterogeneities (Ref 42). The crystallite size of the Al_2O_3 powder which is corundum presents as coarse with calculated size being 141 ± 4 nm. However, after deposition the crystalline content of the coating that has transformed to gamma- Al_2O_3 presents refined crystallite size of 48 ± 2 nm; this seems to cause peak broadening on the high 2θ angle peaks between 100° and 130° . The mechanism of the phase formation in SHVOF-thermal-sprayed alumina has been explained in our previous work (Ref 6).

The observed microstructure of the coating also impacts on its measured properties. The nanohardness measured in the as-sprayed Al_2O_3 coating represents the hardness of

individual lamella—the indents were small enough to fit within a lamella. The nanohardness has higher value compared to the micro-hardness which is lower by ~ 5 GPa; this can be attributed to the high density of each lamella as seen on the fractograph. The micro-indents cover multiple lamellae and inter-lamellae defects (voids, micro-cracks)—the defects reduce the measured micro-hardness (Ref 43). More so, the presence of defects like micro-cracks (vertical and horizontal) and inter-particle voids will interfere with the measured micro-hardness of the coating—the large micro-indents will encompass defects and sintered particles. In addition, particle size refinement can increase the hardness of a non-work hardened material by grain boundary strengthening due to Hall–Petch effect (Ref 44). Typical coating is built up from lamellae, while the lamellae consist of overlaid splats formed from droplets (Ref 45). Dense lamellae are formed from splats with high inter-splat contact area (Ref 46). Turunen et al. (Ref 46) has demonstrated that the indentation modulus of thermally sprayed coatings correlates with its density. The average indentation modulus of the coating reflects the nature of its building blocks—it has a high indentation modulus of 200 ± 7 GPa indicative of its dense building block—the lamellae.

Residual Stress Distribution

The residual stresses from incremental hole-drilling and x-ray diffraction technique have been presented to provide insight into the residual stress behavior of a SHVOF-thermal-sprayed coating built from lamellae. The hole-drilling technique profiles the stress information through the coatings from depths near the surface of the coating; it combines the contribution of all the constituents of a coating—the amorphous phase, the crystalline phases, and the defects in terms of pores and micro-cracks. X-ray diffraction, however, provides an approximate surface stress needed to understand the immediate response of the coating to its functional environment. The hole-drilling technique assumes homogeneity of the distribution of the constituents in the coatings (Ref 17)—as in a bulk sample. However, thermal spray coatings are often built from overlaid lamellae and/or particles would have property variation across their thickness as it has been shown for the coating studied in this case. The differences in the calculated stresses can be narrowed down through a closer inspection by estimating the average of the stress profile obtained from the hole-drilling measurements. Bolelli et al. (Ref 15) has used this approach to present stresses measured by x-ray diffraction and the hole-drilling technique. Table 3 shows the x-ray diffraction stresses and the average of the stresses measured by the hole-drilling technique.

Table 3 Results of the x-ray residual stress compared to the average of the hole-drilling residual stress: σ_{0° and σ_1 are longitudinal stresses, while σ_{90° and σ_3 represent transverse stresses

Coating	X-ray		Hole-drilling	
	σ_{0° (MPa)	σ_{90° (MPa)	σ_1 (MPa)	σ_3 (MPa)
Al ₂ O ₃	− 8.3	25.3	− 162	− 104

The two techniques suggest the Al₂O₃ coating is mostly in compression though to varying degrees in different depths.

Deposition process and property mismatch are the sources of the four types of stresses identified in thermal spray coatings. The deposition process is the source of the quenching (tensile), the peening (compressive), and the phase transformation stress (tensile/compressive), while the thermal stresses (tensile/compressive) results from the coefficient of thermal expansion (CTE) mismatch between the coating and the substrate (Ref 27). The nature of the stresses found in a coating, whether compressive or tensile, would suggest if any of the two sources of the stresses can be considered dominant (Ref 47). The quenching stress (tensile) contribution to the residual stress in the as-sprayed Al₂O₃ coating can be deemed reduced given the poor inter-lamellae bonding identified through the fracture surface, micro-cracks between adjacent lamellae and inter-layer passes—inter-layer defects help in stress redistribution. More so, because the Al₂O₃ coating is built from large overlaid lamellae (> 10 μm , see Figure (Ref 5)) with good intra-lamellae bonding; each lamella then act as distinct entities such that when the whole lamellae experience cooling and shrinkage, the tensile stress generated is released through the inter-lamellae micro-cracks. This phenomenon has been reported for Al₂O₃ coating with similar large lamellae makeup (Ref 15). The peening stress contribution remains significant given the continuous impact of overlaid splats at hypersonic speeds which leaves the overall coating in compression. The collision of splats in this case can be considered inelastic where most of the kinetic energy of the arriving splats is transferred to the underlying splats—both the top and bottom splats spread out stuck together in a composite pile compressed. This is further justified by the average of the measured residual stresses in the Al₂O₃ coating as − 162 MPa (compression) in the longitudinal direction and − 104 MPa (compression) in the transverse direction. There could also be some compressive stress contribution from the phase transformation stress based on the microstructure of the coating described in “Coating Microstructure” section. Considering the coating as a composite mix of amorphous Al₂O₃ matrix reinforced with crystalline Al₂O₃ (gamma and alpha), the amorphous Al₂O₃ in the coating will compress

the sparsely distributed crystalline phases which makes $\sim 20\%$ of the entire mix. This is so in that amorphized material exerts compressive stresses on its surrounding due to its increased disorderliness and volumetric expansion (Ref 48). In addition, the contribution of the thermal stress resulting from the cooling of the combine coating–substrate composites is compressive given that the substrate–coating CTE ratio was ~ 2.1 (Ref 49, 50). In summary, none of the two sources for the four types of stress is dominant for the coating presented in this work. However, of the four types of stress identified in the coating presented in this work, the peening stress and the thermal stress can be considered dominant through the depths of the coating given the CTE ratio of the substrate–coating composite and that the deposition process was HVOF based.

The x-ray diffraction technique has capability to measure the unique residual stress due to crystalline phase transformation when compared to the hole-drilling technique. The difference in the residual stress measured through the x-ray diffraction in σ_{0° (longitudinal) and σ_{90° (transverse) directions is unrelated to the shape or the dimensions of the sample. As evidenced from Fig. 8, the differences between residual stress in the longitudinal and transverse directions—measured through the hole-drilling technique—are well within the error range of the measurements. This concludes that similar stress profile exists in both longitudinal and transverse directions of this coating; however, in the x-ray diffraction residual stress measurement there is a small difference (33 MPa) in the value of residual stress between the transverse and the longitudinal directions. It is not entirely clear why the difference exists, but it should be worth pointing out that only gamma alumina (844) hkl plane was considered in the x-ray diffraction technique and the difference could be down to the crystallographic orientation of this specific plane in two directions.

Conclusions

Residual stress of SHVOF-thermal-sprayed Al₂O₃ coating was investigated using the incremental hole-drilling and the x-ray diffraction technique. It has been demonstrated that SHVOF thermal spray is able to deposit coatings of up to $\sim 200 \mu\text{m}$ with suitable integrity from alumina suspension. The microstructure of the coating shows distinct building elements—lamellae. In regard to the technique used for the residual stress measurement, the through-thickness residual stresses in the coating were obtained from the hole-drilling measurement to be mostly compressive. The shear stress contribution to the hole-drilling residual stress was negligible given that the directional

stress plot shows similar trend as the principal stress plot. The x-ray diffraction technique, on the other hand, provided the contribution of the phase transformation stress to the residual stress in the coating. Besides, the x-ray diffraction residual stress presents the approximate surface stress needed to understand the immediate response of the coating to its functional environment.

Acknowledgments This work was supported by the Engineering and Physical Sciences Research Council (Grant Number EP/M01536X/1). Mr R. Screaton and Mr J. Kirk helped with the spraying of the coatings. Dr Z. Pala helped in the phase analysis of the materials and coatings. The authors thank the Nanoscale and Microscale Research Centre (nmRC) for providing access to characterization instruments. Tunji Owoseni is supported by Petroleum Technology Development Fund (PTDF/ED/PHD/OTA/872) under the overseas scholarship scheme.

Open Access This article is licensed under a Creative Commons Attribution 4.0 International License, which permits use, sharing, adaptation, distribution and reproduction in any medium or format, as long as you give appropriate credit to the original author(s) and the source, provide a link to the Creative Commons licence, and indicate if changes were made. The images or other third party material in this article are included in the article's Creative Commons licence, unless indicated otherwise in a credit line to the material. If material is not included in the article's Creative Commons licence and your intended use is not permitted by statutory regulation or exceeds the permitted use, you will need to obtain permission directly from the copyright holder. To view a copy of this licence, visit <http://creativecommons.org/licenses/by/4.0/>.

References

1. J.R. Davis, Ed., *Handbook of Thermal Spray Technology*, ASM International, USA, 2004
2. M. Niittymäki, K. Lahti, T. Suhonen, and J. Metsajoki, Dielectric Breakdown Strength of Thermally Sprayed Ceramic Coatings: Effects of Different Test Arrangements, *J. Therm. Spray Technol.*, 2015, **24**(3), p 542-551
3. L. Pawlowski, *The Science and Engineering of Thermal Spray Coatings*, 2nd ed., Wiley, West Sussex, 2008, p 597
4. J.W. Murray, G.A. Rance, F. Xu, and T. Hussain, Alumina-Graphene Nanocomposite Coatings Fabricated by Suspension High Velocity Oxy-Fuel Thermal Spraying for Ultra-Low-Wear, *J. Eur. Ceram. Soc.*, 2018, **38**(4), p 1819-1828
5. W. Fan, Y. Bai, J.R. Li, Y. Gao, H.Y. Chen, Y.X. Kang et al., Microstructural Design and Properties of Supersonic Suspension Plasma Sprayed Thermal Barrier Coatings, *J. Alloy. Compd.*, 2017, **699**, p 763-774
6. T.A. Owoseni, J.W. Murray, Z. Pala, E.H. Lester, D.M. Grant, and T. Hussain, Suspension High Velocity Oxy-Fuel (SHVOF) Spray of Delta-Theta Alumina Suspension: Phase Transformation and Tribology, *Surf. Coat. Technol.*, 2019, **371**, p 97-106
7. P. Fauchais, M. Fukumoto, A. Vardelle, and M. Vardelle, Knowledge Concerning Splat Formation: An Invited Review, *J. Therm. Spray Technol.*, 2004, **13**(3), p 337-360
8. S. Kuroda and T.W. Clyne, The Quenching Stress in Thermally Sprayed Coatings, *Thin Solid Films*, 1991, **200**(1), p 49-66
9. J. Matejicek, S. Sampath, D. Gilmore, and R. Neiser, In Situ Measurement of Residual Stresses and Elastic Moduli in Thermal Sprayed Coatings: Part 2: Processing Effects on Properties of Mo Coatings, *Acta Mater.*, 2003, **51**(3), p 873-885
10. A.F.M. Arif, K.S. Al-Athel, and J. Mostaghimi, Residual Stresses in Thermal Spray Coating, *Comprehensive Materials Finishing*, Vol 3, M.S.J. Hashmi, Ed., Elsevier Inc, Amsterdam, 2017, p 56-70
11. P.J. Withers and H.K.D.H. Bhadeshia, Residual Stress. Part 2: Nature and Origins, *Mater. Sci. Technol. Lond.*, 2013, **17**(4), p 366-375
12. D.L. Coats and A.D. Krawitz, Effect of Particle Size on Thermal Residual Stress in WC-Co Composites, *Mater. Sci. Eng., A*, 2003, **359**(1), p 338-342
13. G. Bolelli, L. Lusvardi, T. Varis, E. Turunen, M. Leoni, P. Scardi et al., Residual Stresses in HVOF-Sprayed Ceramic Coatings, *Surf. Coat. Technol.*, 2008, **202**(19), p 4810-4819
14. G. Bolelli, B. Bonferroni, V. Cannillo, R. Gadow, A. Killinger, L. Lusvardi et al., Wear Behaviour of High Velocity Suspension Flame Sprayed (HVSFS) Al_2O_3 Coatings Produced Using Micron- and Nano-Sized Powder Suspensions, *Surf. Coat. Technol.*, 2010, **204**(16-17), p 2657-2668
15. G. Bolelli, V. Cannillo, R. Gadow, A. Killinger, L. Lusvardi, T. Manfredini et al., Properties of Al_2O_3 Coatings by High Velocity Suspension Flame Spraying (HVSFS): Effects of Injection Systems and Torch Design, *Surf. Coat. Technol.*, 2015, **270**, p 175-189
16. N.M. Faisal, R. Ahmed, A.K. Prathuru, S.P. Katikaneni, M.F.A. Goosen, S.Y. Zhang, *Neutron Diffraction Residual Strain Measurements of Molybdenum Carbide-Based Solid Oxide Fuel Cell Anode Layers with Metal Oxides on Hastelloy X*. Experimental Mechanics 2017
17. R. Ahmed, M.E. Fitzpatrick, and N.H. Faisal, A Comparison of Neutron Diffraction and Hole-Drilling Residual Strain Measurements in Thermally Sprayed Coatings, *Surf. Coat. Technol.*, 2012, **206**(19-20), p 4180-4185
18. J. Matejicek and S. Sampath, In Situ Measurement of Residual Stresses and Elastic Moduli in Thermal Sprayed Coatings—Part 1: Apparatus and Analysis, *Acta Mater.*, 2003, **51**(3), p 863-872
19. J. Zhu, H. Xie, Z. Hu, P. Chen, and Q. Zhang, Residual Stress in Thermal Spray Coatings Measured by Curvature Based on 3D Digital Image Correlation Technique, *Surf. Coat. Technol.*, 2011, **206**(6), p 1396-1402
20. J.W. Murray, A.S.M. Ang, Z. Pala, E.C. Shaw, and T. Hussain, Suspension High Velocity Oxy-Fuel (SHVOF)-Sprayed Alumina Coatings: Microstructure, Nanoindentation and Wear, *J. Therm. Spray Technol.*, 2016, **25**(8), p 1700-1710
21. M. Bai, H. Maher, Z. Pala, and T. Hussain, Microstructure and Phase Stability of Suspension High Velocity Oxy-Fuel Sprayed Yttria Stabilised Zirconia Coatings from Aqueous and Ethanol Based Suspensions, *J. Eur. Ceram. Soc.*, 2018, **38**(4), p 1878-1887
22. P. Scardi and M. Leoni, Whole Powder Pattern Modelling, *Acta Crystallogr. Sect. A*, 2002, **58**(2), p 190-200
23. G.M. Pharr, J.H. Strader, and W.C. Oliver, Critical Issues in Making Small-Depth Mechanical Property Measurements by Nanoindentation with Continuous Stiffness Measurement, *J. Mater. Res.*, 2011, **24**(3), p 653-666
24. Z. Zong, J. Lou, O.O. Adewoye, A.A. Elmustafa, F. Hammad, and W.O. Soboyejo, Indentation Size Effects in the Nano- and Micro-hardness of FCC Single Crystal Metals, *Mater. Sci. Eng. A Struct.*, 2006, **434**(1-2), p 178-187
25. P.V. Grant, J.D. Lord, P.S. Whitehead*, *The Measurement of Residual Stresses by the Incremental Hole Drilling Technique*. National Physical Laboratory; 2006. Contract No.: PDB: 3260
26. G.S. Schajer, Measurement of Non-uniform Residual-Stresses Using the Hole-Drilling Method. 1. Stress Calculation Procedures, *J. Eng. Mater. Trans. ASME*, 1988, **110**(4), p 338-343

27. J. Matejicek, S. Sampath, and J. Dubsky, X-Ray Residual Stress Measurement in Metallic and Ceramic Plasma Sprayed Coatings, *J. Therm. Spray Technol.*, 1998, **7**(4), p 489-496
28. M.E. Fitzpatrick, P. Holdway, F.A. Kandil, J. Shackleton, L. Suominen, *Determination of Residual Stresses by X-Ray Diffraction-Issue 2*. Middlesex, United Kingdom: National Physical Laboratory; 2005
29. P.S. Prevéy, X-Ray Diffraction Residual Stress Techniques, *Met. Handb.*, 1986, **513**, p 380-392
30. G. Bolelli, J. Rauch, V. Cannillo, A. Killinger, L. Lusvarghi, and R. Gadow, Microstructural and Tribological Investigation of High-Velocity Suspension Flame Sprayed (HVSFS) Al₂O₃ Coatings, *J. Therm. Spray Technol.*, 2008, **18**(1), p 35
31. G. Sivakumar, R.O. Dusane, and S.V. Joshi, A Novel Approach to Process Phase Pure Alpha-Al₂O₃ Coatings by Solution Precursor Plasma Spraying, *J. Eur. Ceram. Soc.*, 2013, **33**(13–14), p 2823-2829
32. S. Chadha, R. Jefferson-Loveday, and T. Hussain, Effect of Nozzle Geometry on the Gas Dynamics and Evaporation Rates of Suspension High Velocity Oxy Fuel (SHVOF) Thermal Spray: A Numerical Investigation, *Surf. Coat. Technol.*, 2019, **371**, p 78-89
33. A. Killinger, P. Müller, and R. Gadow, What Do We Know, What are the Current Limitations of Suspension HVOF Spraying?, *J. Therm. Spray Technol.*, 2015, **24**(7), p 1130-1142
34. S. Chadha, R. Jefferson-Loveday, T. Hussain, *Effect of Nozzle Geometry on the Gas Dynamics and Evaporation Rates of Suspension High Velocity Oxy Fuel (SHVOF) Thermal Spray: A Numerical Investigation*. Surface and Coatings Technology. 2018.
35. G. Bolelli, V. Cannillo, R. Gadow, A. Killinger, L. Lusvarghi, J. Rauch et al., Effect of the Suspension Composition on the Microstructural Properties of High Velocity Suspension Flame Sprayed (HVSFS) Al₂O₃ Coatings, *Surf. Coat. Technol.*, 2010, **204**(8), p 1163-1179
36. S. Chadha, R. Jefferson-Loveday, F. Venturi, and T. Hussain, A Computational and Experimental Investigation into Radial Injection for Suspension High Velocity Oxy-Fuel (SHVOF) Thermal Spray, *J. Therm. Spray Technol.*, 2019, **28**(6), p 1126-1145
37. R. Rampon, O. Marchand, C. Filiatre, and G. Bertrand, Influence of Suspension Characteristics on Coatings Microstructure Obtained by Suspension Plasma Spraying, *Surf. Coat. Technol.*, 2008, **202**(18), p 4337-4342
38. A. Killinger, 4—Status and Future Trends in Suspension Spray Techniques A2—Espallargas, Nuria. Future Development of Thermal Spray Coatings: Woodhead Publishing; 2015. p. 81–122
39. A. Coghe and G.E. Cossali, Quantitative Optical Techniques for Dense Sprays Investigation: A Survey, *Opt. Lasers Eng.*, 2012, **50**(1), p 46-56
40. C.S. Lee and R.D. Reitz, Effect of Liquid Properties on the Breakup Mechanism of High-Speed Liquid Drops, *Atom. Spray.*, 2001, **11**(1), p 1-19
41. Z. Dai and G.M. Faeth, Temporal Properties of Secondary Drop Breakup in the Multimode Breakup Regime, *Int. J. Multiph. Flow*, 2001, **27**(2), p 217-236
42. T. Ungár, Microstructural Parameters from X-Ray Diffraction Peak Broadening, *Scr. Mater.*, 2004, **51**(8), p 777-781
43. E. Turunen, T. Varis, T.E. Gustafsson, J. Keskinen, T. Fält, and S.-P. Hannula, Parameter Optimization of HVOF Sprayed Nanostructured Alumina and Alumina–Nickel Composite Coatings, *Surf. Coat. Technol.*, 2006, **200**(16–17), p 4987-4994
44. A.H.F. Taha, Application of the Hall-Petch Relation to Microhardness Measurements on Al, Cu, Al-MD 105, and Al-Cu Alloys, *Physica Status Solidi (a)*, 1990, **119**(2), p 455-462
45. N. Espallargas., Introduction to Thermal Spray Coatings. Future Development of Thermal Spray Coatings: Woodhead Publishing; 2015. p. 1–13
46. E. Turunen, T. Varis, S.P. Hannula, A. Vaidya, A. Kulkarni, J. Gutleber et al., On the Role of Particle State and Deposition Procedure on Mechanical, Tribological and Dielectric Response of High Velocity Oxy-Fuel Sprayed Alumina Coatings, *Mater. Sci. Eng., A*, 2006, **415**(1–2), p 1-11
47. J. Matejicek, S. Sampath, P.C. Brand, and H.J. Prask, Quenching, Thermal and Residual Stress in Plasma Sprayed DEPOSITS: NiCrAlY and YSZ Coatings, *Acta Mater.*, 1999, **47**(2), p 607-617
48. G. Parsard, G. Subhash, and P. Jannotti, Amorphization-Induced Volume Change and Residual Stresses in Boron Carbide, *J. Am. Ceram. Soc.*, 2018, **101**(6), p 2606-2615
49. G. Bolelli, V. Cannillo, C. Lugli, L. Lusvarghi, and T. Manfredini, Plasma-Sprayed Graded Ceramic Coatings on Refractory Materials for Improved Chemical Resistance, *J. Eur. Ceram. Soc.*, 2006, **26**(13), p 2561-2579
50. R. Gadow, M.J. Riegert-Escribano, and M. Buchmann, Residual Stress Analysis in Thermally Sprayed Layer Composites, Using the Hole Milling and Drilling Method, *J. Therm. Spray Technol.*, 2005, **14**(1), p 100-108

Publisher's Note Springer Nature remains neutral with regard to jurisdictional claims in published maps and institutional affiliations.